J Mater Sci (2006) 41:5559–5568
DOI 10.1007/s10853-006-0343-x

The relationships between microstructure and crystal structure in zincite solid solutions

T. Yamashita · R. Hansson · P. C. Hayes

Received: 4 September 2005 / Accepted: 30 September 2005 / Published online: 20 June 2006

Abstract Single phase $(Zn,Fe)_{1-x}O$ zincite solid solution samples have been prepared by high temperature equilibration in air and in reducing atmospheres, followed by quenching to room temperature. The Fe^{2+}/Fe^{3+} concentrations in the samples have been determined using wet chemical and XPS techniques. Iron is found to be present in zincite predominantly in the form of Fe^{3+} ions. The transition from an equiaxed grain morphology to plate-like zincite crystals is shown to be associated with increasing Fe^{3+} concentration, increasing elongation in <001> of the hexagonal crystals and increasing anisotropic strain along the *c*-axis. The plate-like crystals are shown to contain planar defects and zincite polytypes at high iron concentrations.

Introduction

Zinc oxide is used in a wide range of industrial applications, such as, diluted magnetic semiconductors [1], gas sensor devices [2], transparent electrodes [3] and piezoelectric devices [4]. The stable form of ZnO is zincite, which has a hexagonal close-packed crystal structure: space group $P6_3mc$, with lattice parameter a = 3.24982(9) Å, c = 5.20661(15) Å [5, 6]. The Zn^{2+} and O^{2-} ions are tetrahedrally coordinated in this structure. It has been pointed out [7] that, assuming purely ionic bonding, the radius ratio of Zn^{2+} and O^{2-} would favour the formation of a structure of 6-fold rather than 4-fold coordination.

T. Yamashita · R. Hansson · P. C. Hayes (✉)
Pyrometallurgy Research Centre, School of Engineering,
The University of Queensland, Brisbane Q4072, Australia
e-mail: p.hayes@minmet.uq.edu.au

Pure ZnO is reported to have a very narrow range of stoichiometry, and low intrinsic defect concentration [8]. There is some evidence for the formation of interstitial Zn in samples prepared at zinc metal saturation [8].

Research on phase equilibria in the system Zn–Fe–O has shown that iron enters into solid solution in zincite [9]. The extent of this solid solubility of iron in zincite increases from 5 mol% at 1,473 K to 30 mol% at 1,773 K in air [9]. X-ray absorption studies of iron-doped ZnO (Fe/(Zn+Fe) = 0.07) produced by solid state reaction under Ar gas indicate that iron is present as Fe^{2+} in this material [10].

Hansson et al [11] report that between 1,473 K and 1,573 K in air significant changes in the morphology of the $(Zn,Fe)_{1-x}O$ grains occur. Samples equilibrated then quenched from temperatures below 1523 K contained equiaxed $(Zn,Fe)_{1-x}O$ grains, whereas those quenched from the temperatures higher than 1573 K consisted of plate-like $(Zn,Fe)_{1-x}O$ grains having high aspect ratio. The formation of these plate-like grains is particularly important in the production of zinc sinters used in primary metal production, since these grains form an interlocking refractory framework. This framework produces materials with high softening temperatures—microstructures and properties that are desirable for the improvement of performance of the ISP zinc smelting process.

The aims of the present study are to establish the oxidation state of iron in zincite, and to explain the relationship between changes in iron in solid solution in zincite and the resultant product morphology.

Experimental

Selected proportions of 99.5+% pure ZnO, Al_2O_3 and Fe_2O_3 (hematite) powders (Aldrich Pty. Ltd.) were

weighed out and thoroughly mixed using an agate mortar and pestle. About 1 g samples of the mixtures were pressed into discs using a tool steel die. The samples were placed in a platinum crucible and then preheated in an electrical resistance furnace. For $(Zn,Fe)_{1-x}O$ samples treated in air the samples were equilibrated at fixed temperatures between 1,373 and 1,723 K for 20 h and then quenched into iced water. The $(Zn,Al)_{1-y}O$ sample was equilibrated at 1,973 K for 20 h in air and then quenched into iced water.

For the heat treatment in a reducing atmosphere, the powder samples were equilibrated at 1,573 K in a flowing gas mixture containing 39.3% (±0.5 vol%) of 2.07%H_2/97.93%N_2 mixture and 60.7% (±0.5 vol%) of CO_2; under these conditions the oxygen partial pressure is 1×10^{-6} atm at 1,573 K [12]. The fired pellet was broken up to pieces (~1 mm diameter) to expose more surface area then refired in the flowing gas mixture. The quenching in this case was performed by lowering the sample from the hot zone in the vertical furnace. The temperature of the furnace was monitored using a Pt6%Rh/Pt30%Rh thermocouple previously calibrated against a standard supplied by the National Measurement Laboratory (Melbourne, Australia). The temperature of the furnace was controlled within ±5 K.

The compositions of the quenched samples were analysed using JEOL 8800L electron probe microanalyser (EPMA) (JEOL, Tokyo, Japan) with wavelength-dispersive spectrometers. The inbuilt ZAF correction procedure with standard materials, Fe_2O_3 (Charles M Taylor Co., Stanford, CA) and ZnO (prepared ''in-house'' by sintering 99.9+ purity ZnO powder and verified against willemite (Zn_2SiO_4) standard supplied by Micro-Analysis Consultants Ltd., Cambridge, United Kingdom, was utilised for the analysis. The precision of the sample analyses were better than ±1 wt%. The Fe^{2+}/Fe^{3+} ratios in the samples following equilibration were determined by wet chemical analysis and titration using ammonium metavanadate to obtain the Fe^{2+} concentration. The total ion was also measured by titration and the Fe^{3+} concentration obtained by difference. The details of the titration technique are reported elsewhere [11].

The equilibrated samples were mounted in epoxy resin and polished for metallographic examination. After final polishing with 0.3 μm alumina powder, the surface was ultrasonically cleaned in water. The polished surface was then etched in concentrated acetic acid for times of 30 s for pure ZnO, to up to 9 h for samples of high iron concentration in the zincite.

The microstructures of the $(Zn,Fe)_{1-x}O$ solid solution samples were studied using optical microscopy and scanning electron microscopy (SEM) (JSM6400F, JEOL, Tokyo, Japan).

XPS analyses were performed using KRATOS Axis Ultra (Kratos Analytical, Manchester, United Kingdom) on $(Zn,Fe)_{1-x}O$ with Fe/(Zn+Fe) = 0.186. To avoid oxidation of Fe^{2+} on the surface to Fe^{3+}, the samples were cleaved in high vacuum (~3×10^{-8} torr) before moving directly into the measurement chamber. The incident monochromated X-ray beam from the Al target (15 kV, 10 mA) was focused on a 0.7 mm × 0.3 mm area on the cleaved surface of the sample.

X-ray powder diffraction (XRD) studies were carried out using a Bruker D8 Advance (Bruker AXS, Germany) diffractomator with a graphite monochromator and CuK_α radiation. For X-ray diffraction (XRD) analysis the $(Zn,Fe)_{1-x}O$ pellet samples were crushed and ground using an agate mortar and pestle. The particle size distributions of the ground powders were measured using a Malvern Mastersizer 2000 (Malvern Instruments, United Kingdom). The particle size measurements using Malvern Mastersizer 2000 showed that the mean particle sizes (d50) of the sample powders were approximately 12 μm.

10 wt% Eskolaite, Cr_2O_3 (Standard reference Material 674a, National Institute of Standard, Gaithersburg MD, USA), was mixed with each $(Zn,Fe)_{1-x}O$ sample to provide an internal standard. The preliminary XRD run was made using these samples and the absolute peak positions were determined against the standard peak positions for the standard Cr_2O_3 sample. The XRD spectra for the Rietveld structure refinement were obtained in the 2θ range of 15–120° with step size of 0.02° and scanning rate of 0.5°/min.

Rietveld analysis of the XRD signal peak intensities, peak profiles and peak positions was carried out using the RIETAN-2000 [13], computer package. The Pseudo-Voigt function is used for peak profiles where full width at half maximum (FWHM) of Gaussian part, $H_{KG,}$ and Lorentzian part, H_{KL} [14, 15] are expressed as follows.

$$H_{KG} = [8 \ln 2(U \tan^2 \theta_K + V \tan \theta_K + W + P \sec^2 \theta_K)]^{1/2},$$

$$H_{KL} = (X + X_e \cos \varphi_K) \sec \theta_K + (Y + Y_e \cos \varphi_K) \tan \varphi_K,$$

where θ_K is the Bragg angle, V and W are instrument dependent constants, X and X_e are peak broadening parameters caused by the crystalline size effect, U, Y and Y_e are peak broadening parameters caused by strain (U and Y are for isotropic strain and Y_e is for anisotropic strain) , ϕ_K is the angle between the scattering vector and an anisotropic peak broadening axis.

At first the structure refinement for pure ZnO powder (d_{50} < 1 μm) purchased from Aldrich Pty. Ltd. was carefully carried out using the Rietveld technique, and the refined Rietveld parameters for the pure powder were obtained. For the refinement the parameters were optimised to minimise the residual R_{wp} [16] factor. Throughout the

structure refinement study of the $(Zn,Fe)_{1-x}O$ samples, *V* and *W* (which are both machine dependent parameters) and *B* (isotropic displacement parameter) are fixed during the analysis with the values obtained from the pure ZnO powder as shown in Table 1. The isotropic displacement parameter *B* is the distance that the specified element thermally vibrates, and it is assumed that Zn and Fe atoms have the same value of *B*.

Lattice images of the microstructures were obtained using Tecnai 20 FEG transmission electron microscope (TEM) (Philips, Netherlands) with an acceleration voltage of 200 kV. Three samples, pure ZnO quenched from 1,373 K in air, $(Zn,Fe)_{1-x}O$ with Fe/(Zn+Fe) = 0.061 and 0.186 prepared at 1,723 K in air, and $(Zn,Al)_{1-y}O$ with Al/(Zn+Al) = 0.039 prepared at 1,973 K in air, were chosen for the study. These samples were ground with an agate mortar and pestle and then mixed with a small amount of acetone. The mixture was placed onto the carbon reinforced holey micro grid using a pipet and the sample was dried in air.

Results

Microstructure

Optical and secondary electron micrographs of the $(Zn,Fe)_{1-x}O$ prepared in air at 1,723 K are shown in Fig 1a–c. The pure ZnO prepared under these conditions consists of equiaxed grains with the grain size more than 100 μm. For the same sintering temperature and time, as the iron concentration is progressively increased, the grain sizes decrease and the grains become more platelike or acicular in shape. Etching of the samples reveals (Fig. 2) that, in the iron containing zincite samples, each grain contains a plate-like sub-structure not visible in unetched samples. The distance between the plates in the sub-structure also becomes smaller as the iron concentration in the samples is increased. Similar findings were obtained in $(Zn,Fe)_{1-x}O$ samples prepared under reducing conditions.

The mean aspect ratios of $(Zn,Fe)_{1-x}O$ grains as a function of total iron concentration are shown in Fig. 3.

Table 1 Refined Rietveld parameters for pure ZnO

Gaussian FWHM parameter, *U*	3.09E-04
Gaussian FWHM parameter, *V*	–6.85E-05
Gaussian FWHM parameter, *W*	1.38E-03
Scherrer coefficient for Gaussian broadening, *P*	0
Lorentzian Scherrer broadening *X*	7.19E-02
Anisotropic Scherrer broadening, X_e	0
Strain broadening, *Y*	5.95E-02
Anisotropic strain broadening, Y_e	0
Preferred-orientation parameter, *r*	0.992216
Lattice parameter, *a*	3.25254
Lattice parameter, *b*	3.25254
Lattice parameter, *c*	5.21108
Lattice parameter, α	90
Lattice parameter, β	90
Lattice parameter, γ	120
Overall isotropic displacement parameter, *Q*	0
Oxygen atom Occupation factor, *g*	1
Fractional coordinate, *x*	0.333333
Fractional coordinate, *y*	0.666667
Fractional coordinate, *z*	0.375
Isotropic displacement parameter, *B*	0.27367
Zinc atom Occupation factor, *g*	1
Fractional coordinate, *x*	0.666667
Fractional coordinate, *y*	0.333333
Fractional coordinate, *z*	0.5
Isotropic displacement parameter, *B*	0.54388

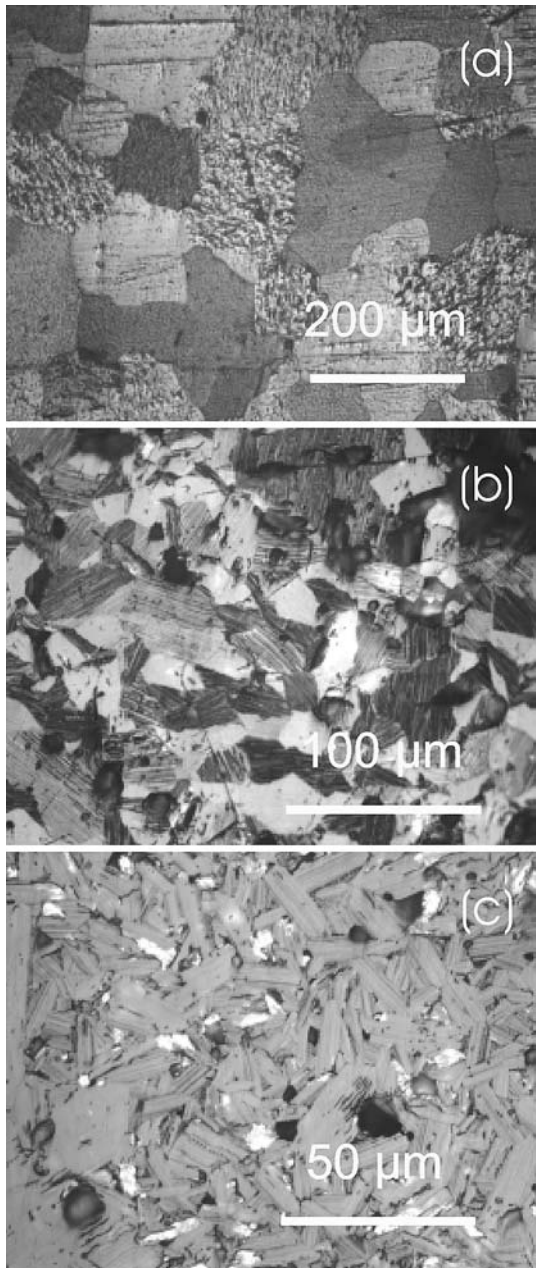

Fig. 1 Optical micrographs of $(Zn,Fe)_{1-x}O$ prepared at 1,723 K in air with Fe/(Zn+Fe) = (**a**) 0.000, (**b**) 0.012 and (**c**) 0.018. (etched in acetic acid)

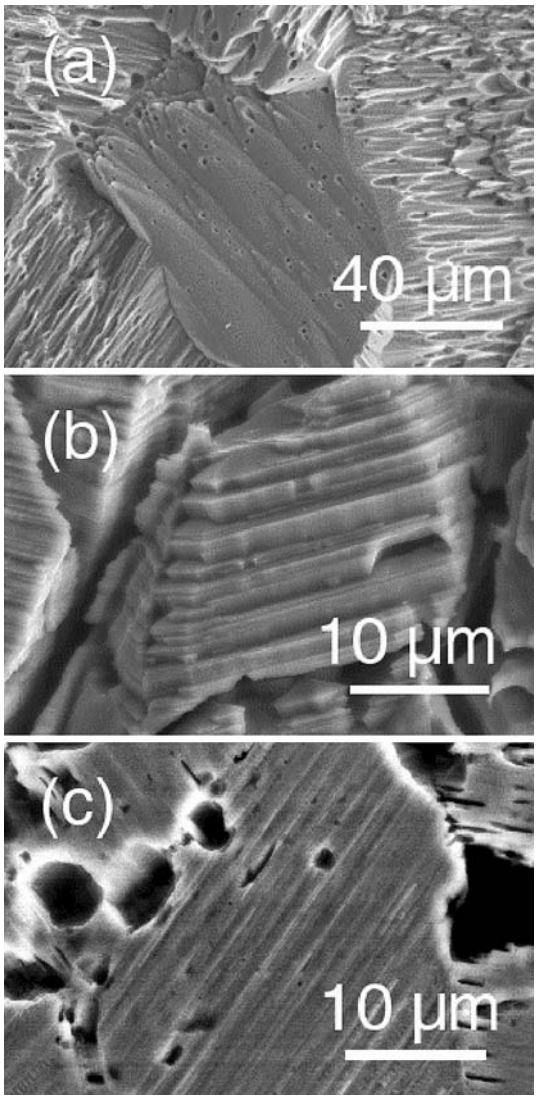

Fig. 2 SEM micrographs of $(Zn,Fe)_{1-x}O$ prepared at 1,723 K in air with Fe/(Zn+Fe) = (**a**) 0.000, (**b**) 0.012 and (**c**) 0.018. (etched in acetic acid)

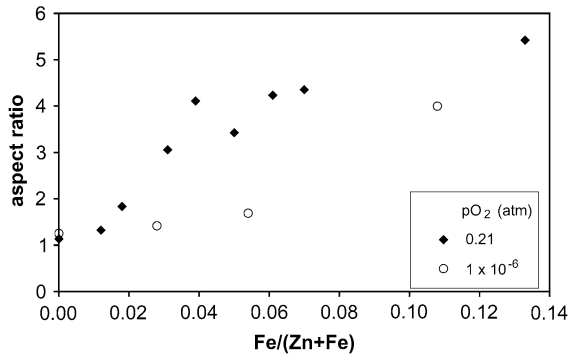

Fig. 3 The dependence of the aspect ratios of zincite grains on composition and oxygen partial pressure. (pO_2 = 0.21 atm at 1,723 K and $pO_2 = 1 \times 10^{-6}$ atm at 1,573 K)

The samples prepared in air (pO_2 = 0.21 atm) were fired at 1,723 K and the samples prepared in the reducing condition ($pO_2 = 1 \times 10^{-6}$ atm) were fired at 1,573 K. In both oxidising and reducing conditions the aspect ratio is approximately unity at low Fe concentrations and then steadily increases with increasing total Fe concentration. The total iron concentration at which the aspect ratio begins to increase differs between samples produced in air and those prepared under reducing conditions. The grain morphology of the $(Zn,Al)_{1-y}O$ sample in air was equiaxed.

Crystal structure

Pure ZnO pellets were fired at 1,498, 1,523, 1,548, 1,573, 1,673 and 1,723 K in air and quenched into iced water. The crystal structures of these samples were examined using the XRD/Rietveld method. In the present study the lattice parameters obtained from all of these quenched pure ZnO samples are identical of $a = 3.2505$ (±0.0021)Å and $c = 5.2052$ (± 0.0034)Å. These values show very good agreement with those given in JCPDS, where a is 3.24982(9)Å and c is 5.20661(15)Å [5]. Refined parameters using RIETAN2000, such as Full-Width at Half-Maximum (FWHM) parameters, peak shape related parameters (Asymmetry parameters, Mixing parameters, etc), are also identical, within experimental uncertainty, in all of these pure ZnO samples.

Fe^{2+} and Fe^{3+} in zincite

Following high temperature equilibration the samples were analysed using EPMA, wet chemical and XPS techniques. The compositions of the final pellets are given in Table 2. For the EPMA measurements, these values represent the mean of the compositions determined by averaging the measurements obtained from 10 different positions within the sample. The standard deviations in the analyses for these data were less than 1%. The composition of the $(Zn,Al)_{1-y}O$ sample was analysed to be Al/(Zn+Al) = 0.039 using EPMA.

The results of the titration analysis of the $(Zn,Fe)_{1-x}O$ samples reveal (Fig. 4) that, at low total iron concentrations Fe/(Zn+Fe) ≤ 0.01 in air and ≤0.104 under reducing conditions, the iron is principally present as Fe^{2+}. At higher total iron concentrations the iron is principally present as Fe^{3+}. The Fe:Zn ratios obtained from both EPMA and titration techniques are in good agreement. Hereafter, the Fe/(Zn+Fe) ratios obtained from the titration technique are used for identifying the samples.

XPS analysis was carried out for the sample $(Zn,Fe)_{1-x}O$ with Fe/(Zn+Fe) = 0.186. The XPS pattern for Fe_{2p} shown

Table 2 Compositioinal analysis of $(Zn,Fe)_{1-x}O$ solid solutions

	Molar Compositions (EPMA)			Compositions (titration technique)			
Prepared in air	Sample name	Fe	Zn	Fe^{2+}	Fe^{3+}	Fe/(Zn + Fe)	Zn^{2+}
	R241	0.00	1.000	0.000	0.000	0.000	1.000
	R95	0.11	0.989	0.008	0.004	0.012	0.988
	R96	0.017	0.983	0.008	0.010	0.018	0.982
	R97(A)	0.030	0.970	0.009	0.022	0.031	0.969
	R98	0.038	0.962	0.009	0.030	0.038	0.962
	R99	0.049	0.951	0.009	0.041	0.050	0.950
	R100	0.060	0.940	0.010	0.051	0.060	0.940
	R101	0.069	0.931	0.010	0.060	0.070	0.930
	R91	0.133	0.867	0.007	0.126	0.133	0.867
	R92	0.130	0.870	0.008	0.122	0.130	0.870
	R93	0.138	0.862	0.011	0.127	0.139	0.861
	R102	0.173	0.827	0.015	0.158	0.173	0.827
	R103	0.186	0.814	0.014	0.172	0.186	0.841
Prepared in the reducing atmosphere	R416	0.000	1.000	0.000	0.000	0.000	1.000
	R417	0.028	0.972	0.028	0.000	0.028	0.972
	R418	0.054	0.946	0.045	0.010	0.055	0.945
	R419	0.108	0.892	0.052	0.056	0.108	0.892
	R420	0.214	0.786	0.073	0.140	0.213	0.787

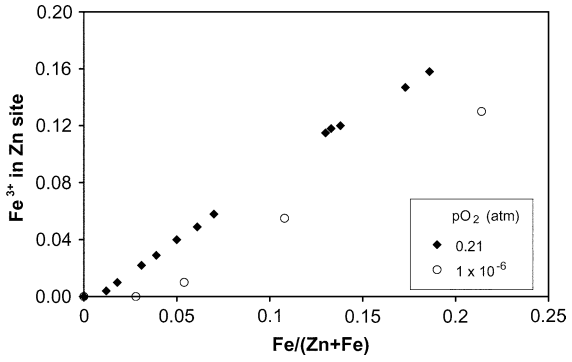

Fig. 4 Fraction of Fe^{3+} ions in $(Zn,Fe)_{1-x}O$. (pO_2 = 0.21 atm at 1,723 K and $pO_2 = 1 \times 10^{-6}$ atm at 1,573 K)

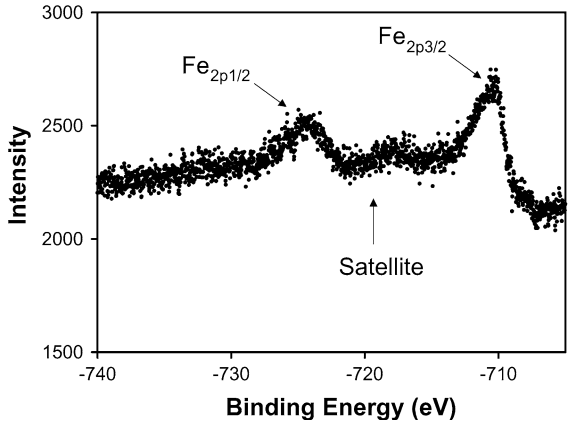

Fig. 5 XPS patterns of Fe_{2p} for $(Zn,Fe)_{1-x}O$ with Fe/(Zn+Fe) = 0.186 prepared in air at 1,723 K, showing the Fe^{3+} satellite peak

in Fig. 5 exhibits two distinct peaks at 710.5 and 724.3 eV for $Fe_{2p3/2}$ and $Fe_{2p1/2}$, respectively. These peak positions are very close to those for pure Fe_2O_3 (hematite) [17] in which all Fe is trivalent, i.e. 710.8 eV for $Fe_{2p3/2}$ and 724.5 eV for $Fe_{2p1/2}$. A smaller but distinct satellite peak is also observed at 718.2 eV in the Fe/(Zn+Fe) = 0.186 as shown in Fig. 5. This is characteristic of Fe^{3+} [17] and thus it clearly shows that the main oxidation state of iron in high iron $(Zn,Fe)_{1-x}O$ solid solutions is trivalent.

Rietveld analysis

The XRD patterns obtained from selected $(Zn,Fe)_{1-x}O$ samples are shown in Fig. 6. As the iron concentration increases,

(a) the intensity of the 100 peak increases relative to the 101 peak.
(b) the 101, 102, 103 peaks become broader.
(c) the 002 peak shifts to lower diffraction angles.
(d) the intensity of the strongest XRD peak (101 or 100 depending on the Fe concentration) reduces from 8000 to 1000 counts.

All of the samples were analysed using the Rietveld technique and the parameters adjusted to minimise the residuals. The results of the structure refinement for the lattice parameters are shown in Fig. 7. The lattice parameters a and b of hexagonal $(Zn,Fe)_{1-x}O$ are found to be independent of the total iron concentration within experimental uncertainty, whilst the lattice parameter c clearly increases with increasing Fe concentration for the samples prepared both in air and in the reducing atmosphere. As

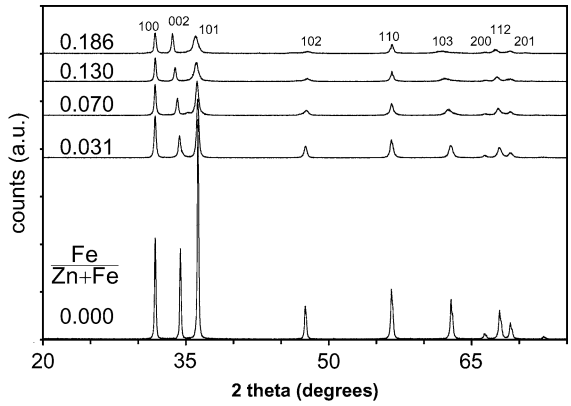

Fig. 6 XRD patterns of $(Zn,Fe)_{1-x}O$ solid solutions prepared at 1,523 K with the compositions, Fe/(Zn+Fe) = 0.000, 0.031, 0.070, 0.130, 0.186, showing changes in relative peak intensity and interplaner spacings. (Cu$K\alpha$ radiation)

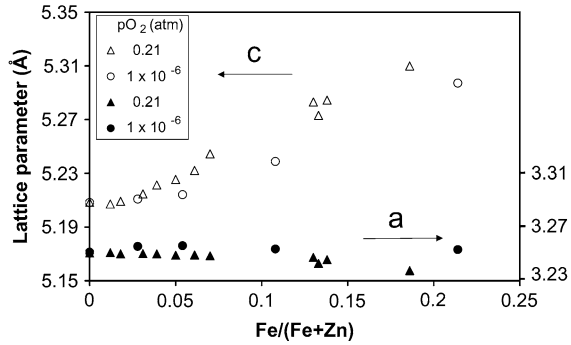

Fig. 7 Lattice parameters of (Fe/(Zn+Fe)) solid solutions. (pO_2 = 0.21 atm at 1,723 K and $pO_2 = 1 \times 10^{-6}$ atm at 1,573 K)

shown in Fig. 7, the *c* lattice parameter remains constant up to Fe/(Zn+Fe) = 0.02 and 0.04 for $(Zn,Fe)_{1-x}O$ prepared in air and the reducing atmosphere, respectively.

As shown in Fig. 6, the 101, 102, 103 peaks are broadened as the iron concentration is increased. Assuming the particle size variation in XRD measurement is not responsible for this phenomenon this indicates that the XRD peak broadening is due to internal defects, such as stacking faults, in the hexagonal close packed materials since the broadened peaks satisfy the condition $h-k = 3n + 1$ ($l \neq 0$) [18]. The intensity of the strongest XRD peak reduces from 8,000 (pure ZnO) to 1,000 ($(Zn,Fe)_{1-x}O$ with Fe/(Zn+Fe) = 0.186), this is an indication that the degree of crystallinity decreases with increasing iron concentration possibly because the presence of Fe ions in $(Zn,Fe)_{1-x}O$ introduces strains and/or defects in the crystal.

Since the Rietveld refinement was carried out using a pseudo-Voigt function [19] for curve fitting, the strain in the lattice can be estimated. The anisotropic strain along <001> as a function of total iron concentration is shown in Fig. 8. It can be seen that the magnitude of the anisotropic

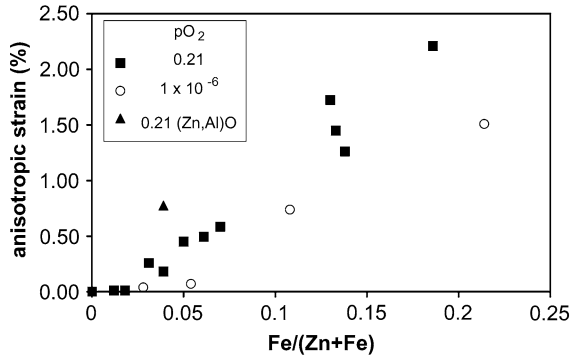

Fig. 8 Anisotropic strain in Fe/(Zn+Fe) solid solution. (pO_2 = 0.21 atm at 1,723 K and $pO_2 = 1 \times 10^{-6}$ atm at 1573 K)

strain relative to that in pure ZnO increases monotonically with increasing iron concentration. Note that the anisotropic strain is very low up to Fe/(Zn+Fe) = 0.02 and 0.04 for the samples prepared in air and in the reducing atmosphere, respectively. The lattice parameters *a* and *c* for $(Zn,Al)_{1-y}O$ at Al/(Zn+Al) = 0.039 at 1973 K are 3.2518(5) and 5.1839(2), respectively. Whilst *a* for $(Zn,Al)_{1-y}O$ is comparable to $(Zn,Fe)_{1-x}O$, *c* for $(Zn,Al)_{1-y}O$ is significantly smaller than that for $(Zn,Fe)_{1-x}O$ (cf. Fig. 7). The anisotropic strain for the $(Zn,Al)_{1-y}O$ sample could not be defined clearly since R_{wp}'s of the Rietveld analysis with a restriction of anisotropic strain zero and without that restriction were the same within the experimental uncertainty.

Lattice images

The internal structures of $(Zn,Fe)_{1-x}O$ samples prepared in air were examined at high resolution using the transmission electron microscope (TEM), (pure ZnO quenched from 1373 K, $(Zn,Fe)_{1-x}O$ with Fe/(Zn+Fe) = 0.060 and 0.186 quenched from 1723 K). The TEM micrographs of zincite with the zone axes of [001] and [100] for each sample are shown in Fig. 9. No significant concentrations of defects such as stacking fault, dislocations or twins were observed in the TEM micrographs for pure ZnO with the zone axes of [001] and [100] (Fig. 9a, b) and $(Zn,Fe)_{1-x}O$ with the zone axes of [001] (Fig. 9c, e). However, the TEM micrographs of $(Zn,Fe)_{1-x}O$ with the zone axes of [100] in Fig. 9d and f clearly show planar defects (stacking faults) along (001) plane dispersed throughout the material. The diffraction patterns in Fig. 9d and f show streaks in the *c* direction. These streaks also indicate defects along (001) plane. The defect planes parallel to the *a–b* plane are observed in some parts of the sample $(Zn,Fe)_{1-x}O$ with Fe/(Zn+Fe) = 0.186 to be ordered; the planar defects are observed to occur at a regular spacing of 36.5 Å as shown in Fig. 10. The corresponding selected area diffraction

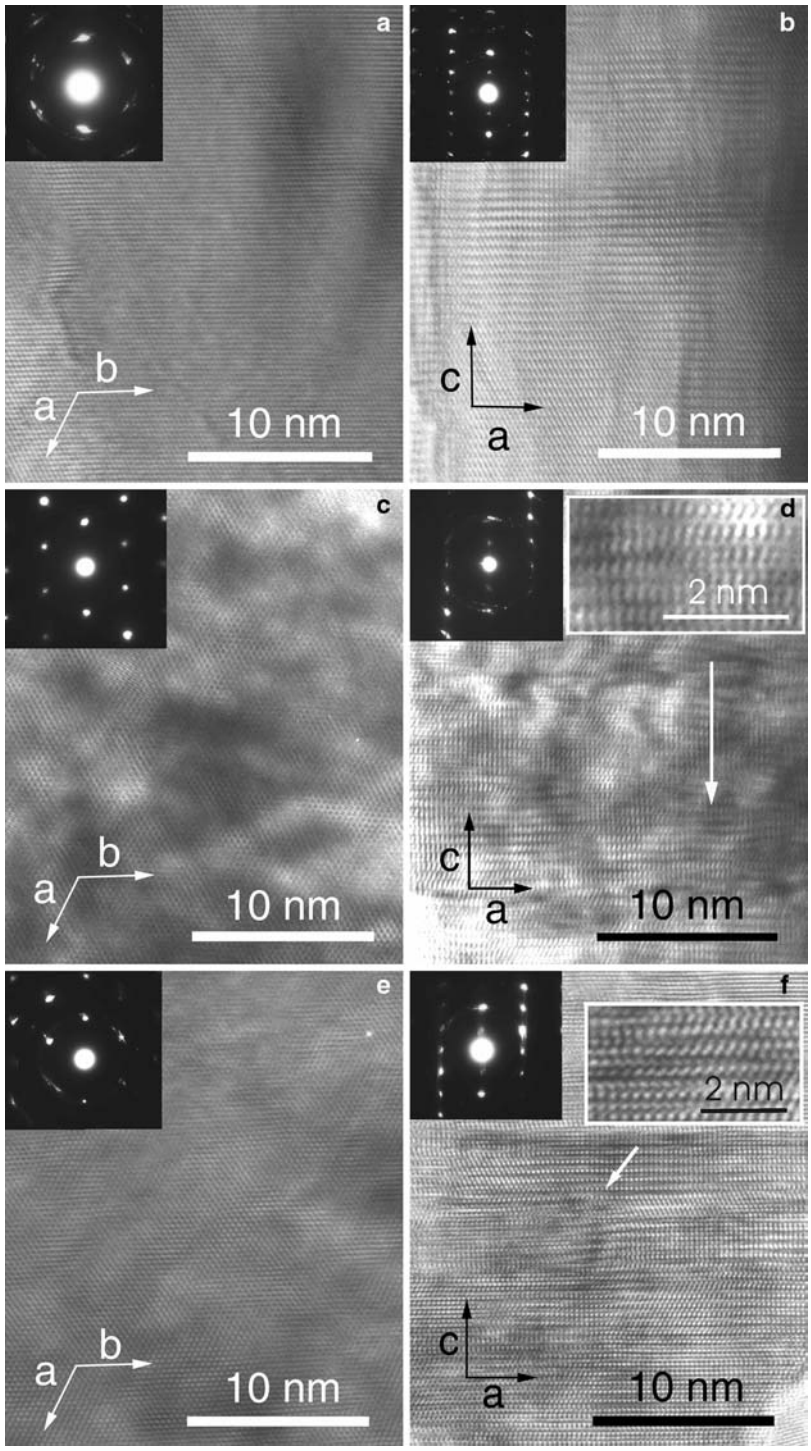

Fig. 9 TEM micrographs for (**a**) pure ZnO with zone axes of [001], (**b**) pure ZnO with zone axes of [100], (**c**) $(Zn,Fe)_{1-x}O$ with Fe/(Zn+Fe) = 0.061 solid solution sample with zone axes of [001], (**d**) $(Zn,Fe)_{1-x}O$ with Fe/(Zn+Fe) = 0.061 solid solution sample with zone axes of [100], (**e**) $(Zn,Fe)_{1-x}O$ with Fe/(Zn+Fe) = 0.186 solid solution sample with zone axes of [001] and (**f**) $(Zn,Fe)_{1-x}O$ with Fe/(Zn+Fe) = 0.186 solid solution sample with zone axes of [100]

(SAD) patterns for these micrographs have 13 extra satellite reflections between (002) and ($00\bar{2}$). These extra diffraction spots originate from the super lattice-like periodic structure in the *c* direction. These results together indicate the formation of a polytype crystal structure expressed as 14H using the Ramsdell notation [20]. However, since the XRD patterns for this sample show no extra peaks, this polytype crystal structure is not present throughout the entire sample.

Figure 11 shows the TEM micrograph for $(Zn,Al)_{1-y}O$ with Al/(Zn+Al) = 0.039 solid solution sample with zone axis of [100]. Compared to Fig. 9d and f, the $(Zn,Al)_{1-y}O$ sample has a much lower concentration of planar defects.

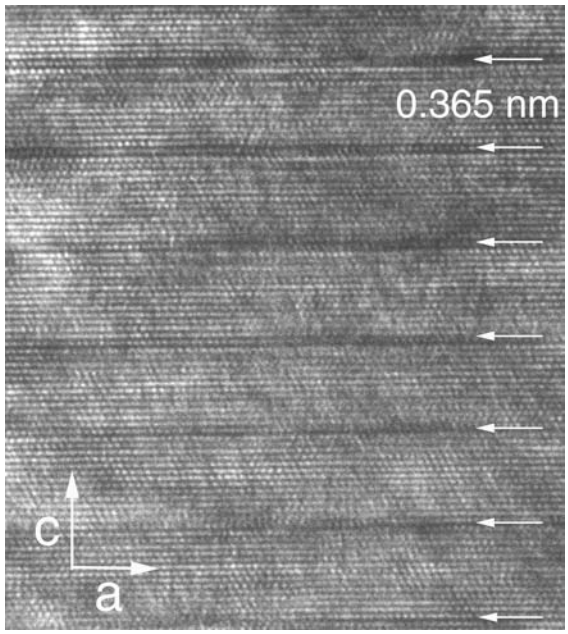

Fig. 10 TEM micrographs for $(Zn,Fe)_{1-x}O$ with Fe/(Zn+Fe) = 0.186 solid solution sample with zone axes of [100]. Showing the presence of polytype structures with a stacking sequence of 0.365 nm

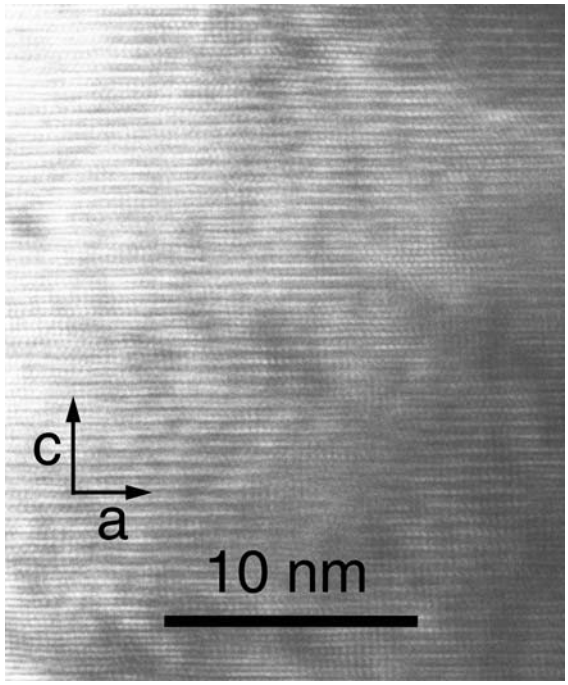

Fig. 11 TEM micrographs for $(Zn,Al)_{1-y}O$ with Al/(Zn+Al) = 0.039 solid solution sample with zone axes of [100]

Discussion

It has been shown in the present investigation that

(i) Iron in $(Zn,Fe)_{1-x}O$ solid solutions is present as Fe^{2+} at low total iron concentrations but that Fe^{3+} becomes the dominant species in high iron zincites (Fig. 4),

(ii) The lattice parameter *c* and the anisotropic strain increase with increasing iron concentration in both oxidising and reducing conditions, and

(iii) The onset of significant changes in crystal anisotropy appears to coincide with increasing Fe^{3+} concentration in the lattice.

From these observations it is apparent that changes in the *c* dimension and crystal anisotropy are associated with the presence of Fe^{3+}. To test this hypothesis the lattice parameter data, anisotropic strain and aspect ratios are replotted against Fe^{3+} concentration rather than total iron for both oxidising and reducing conditions (Figs. 12–15). It can be seen that in each case the data is in agreement with the proposed correlation within experimental uncertainty.

A possible explanation for the *c* lattice parameter elongation with increasing Fe^{3+} concentration is the Jahn–Teller effect [21]. However, the Fe–O bonding in $(Zn,Fe)_{1-x}O$ is tetrahedrally coordinated and thus Fe^{3+} may take the high spin state. Most of tetrahedral complexes are in the high spin state because of the relatively small d orbital splitting (4/9 that of a octahedral complex with similar ligands and bond length) [22]. It appears unlikely therefore that Jahn–Teller effect is the cause of the distortion in the present case.

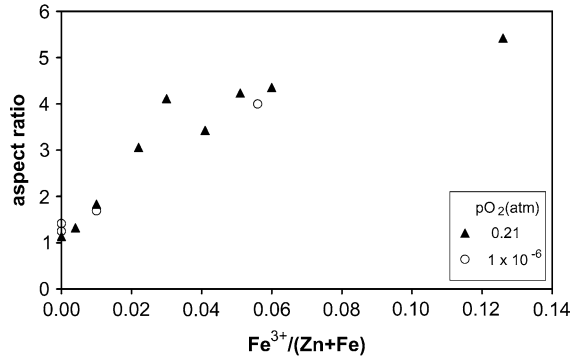

Fig. 12 Aspect ratio of grains as a function of Fe^{3+} (pO_2 = 0.21 atm at 1723 K and $pO_2 = 1 \times 10^{-6}$ atm at 1,573 K)

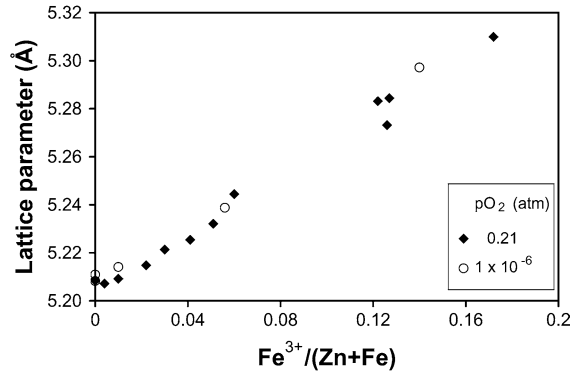

Fig. 13 The *c* lattice parameter in $(Zn,Fe)_{1-x}O$ solid solutions as a function of Fe^{3+} concentration (pO_2 = 0.21 atm at 1,723 K and $pO_2 = 1 \times 10^{-6}$ atm at 1,573 K)

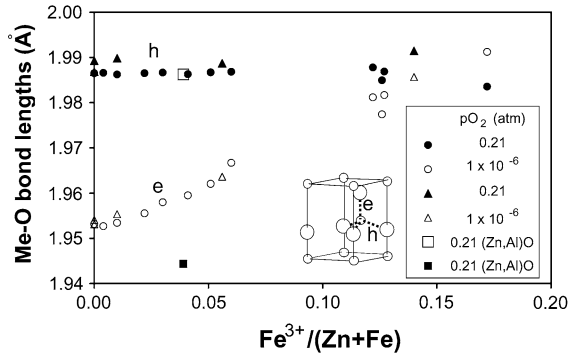

Fig. 14 Anisotropic strain in $(Zn,Fe)_{1-x}O$ solid solutions as a function of Fe^{3+} concentration (pO_2 = 0.21 atm at 1,723 K and $pO_2 = 1 \times 10^{-6}$ atm at 1573 K)

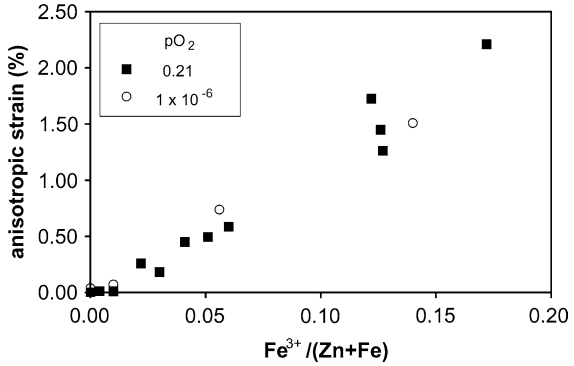

Fig. 15 The mean Me–O bond lengths in $(Zn,Fe)_{1-x}O$ solid solutions as function of Fe^{3+} concentration. The bonds e and h are indicated in the inset ZnO unit cell

The mean Me–O bond lengths obtained from the Rietveld structure refinement of $(Zn,Fe)_{1-x}O$ are plotted against Fe/(Zn+Fe) in Fig. 15. The length of Zn–O(e) is smaller than the Zn–O(h) bonds in pure ZnO. However, because the Zn–O bonds in ZnO are sp^3 hybridized orbits [23], all Zn–O bonds should be symmetrical. This deviation from the symmetry (shorter Zn–O(e)) may be caused by a strong crystal field force [7] (note that Zn–O should be octahedral coordination if only ionic sizes of Zn and O are taken into account [7]). As Zn^{2+} ions are progressively replaced by Fe^{3+}, the mean Zn/Fe–O(e) bond length increases and at the highest Fe doping level investigated in this study, the Zn/Fe–O lengths (e) and (h) are nearly identical. Thus Fe doping may affect the crystal field, making the sp^3 hybridized orbits in the Zn/Fe–O bonds more symmetrical. This symmetrical distribution of the sp^3 hybridized orbits may be the cause of the *c* lattice parameter elongation when more Zn is replaced by Fe.

The Rietveld structure refinements show that Fe^{3+} in ZnO introduces anisotropic strain along *c*-axis, whereas Al^{3+} additions do not show clear evidence of introduction of the anisotropic strain and lead to reduced unit cell sizes. (Note that concentration of Fe^{3+} in the Zn site in the $(Zn,Fe)_{1-x}O$ with Fe/(Zn+Fe) = 0.06 sample (Fig. 9c, d) and that of Al^{3+} in the $(Zn,Al)_{1-y}O$ with Al/(Zn+Al) = 0.039 sample are 0.051 and 0.039, respectively. Though the TEM micrographs do not necessarily represent the mean microstructure of the sample, it may be safely said that no clear evidence was found in the present study that the introduction of Al^{3+} results in any significant amounts of anisotropic strain in the lattice. While Al^{3+} and Fe^{2+} do not elongate the *c* lattice parameter nor Zn–O bond along *c*-axis, Fe^{3+} elongates the *c* lattice parameter significantly and Zn–O bond along *c*-axis, which makes the Zn–O sp^3 hybridised orbit more symmetrical. Since Fe^{2+} has the same valency of Zn, it does not affect sp^3 hybridised orbit. It may be that for Fe^{3+}, 3d level of Fe is close to Zn–O sp^3 hybridised orbit and thus the extra electron is directly given to the sp^3 hybridised orbit and increase the symmetry, whereas the electrons in 2s and 2p orbits in Al are localized and do not affect the sp^3 hybridised orbit in Zn–O. This *c* lattice parameter elongation/sp^3 hybridised orbit symmetrisation together with anisotropic strain along *c*-axis appears to lead to the plate-like grain morphology in $(Zn,Fe)_{1-x}O$.

Summary

A systematic study has been undertaken to determine the oxidation state of iron in $(Zn,Fe)_{1-x}O$ zincite solid solutions in both oxidising and reducing conditions. It has been clearly shown that iron is present as Fe^{2+} at low total iron concentrations. At high temperatures in both oxidising and reducing conditions, the maximum solubility of iron in zincite significantly increases—and iron is found predominantly in the form of Fe^{3+}.

Whilst the presence of Fe^{3+} in the lattice leads to significant lattice strain along <001> of the hexagonal crystal, no clear evidence was found that Al^{3+} introduces anisotropic strain. Only Fe^{3+} leads to the *c* lattice parameter elongation and to more uniform Zn/Fe–O bond lengths. The transition from equiaxed to plate-like crystal morphology appears to be associated with increasing Fe^{3+} in the zincite lattice.

Al^{3+} ions appear to decrease the mean Me–O bond length, favouring the formation of equiaxed zincite crystals.

The present studies explain the formation of a continuous framework zincite structures observed in commercial zinc sintering operations and provide important insights into the effects of system chemistry and process conditions on this phenomenon.

Acknowledgements The authors would like to acknowledge funding for this project from Australian Research Council – Linkage Program, and from industry sources coordinated by ISP Smelting,

UK. They also would like to thank Dr. Koike of Tohoku University for his comments on the TEM micrographs, and the assistance of the Centre for Microscopy and Microanalysis, University of Queensland, with use of electron microscope facilities.

References

1. Fukuyama T, Zhengwu J, Ohtomo A, Koinuma H, Kawasaki M (1999) Appl Phys Lett 75:3366
2. Matsushima S, Abe K, Kobayashi K, Okada G (1992) J Mat Sci Lett 11:1389
3. Igarashi Y, Saito H (1991) J Appl Phys 70:3613
4. Suhara T, Shiono T, Nishihara H, Koyama J (1983) J Lightwave Technol LT1:624
5. McMurdie H (1986) Powder Diffract 1:76
6. Rymer TB, Archardand GD (1952) Research 5:292
7. Yanagida H (1982) Chemistry of ceramics. Maruzen, Tokyo, 18 p
8. Kofstad P (1972) Nonstoichiometry, diffusion, and electrical conductivity in binary metal oxide. Wiley-Interscience
9. Degterov SA, Jak E, Hayes PC, Pelton AD (2001) Metall Mater Trans B 32B:643
10. Han S-J, Song JW, Park SH, Park JH, Jeong YH (2002) Appl Phys Lett 81:4212
11. Hansson R, Hayes PC, Jak E (2004) Scand J Metallurgy v33:294
12. Bale CW, Chartrand P, Degterov SA, Eriksson G, Hack K, Mahfoud RB, Melancon J, Pelton AD, Petersen S (2002) CALPHAD 26(2):189
13. Izumi F, Ikeda T (2000) Mater Sci Forum 198:321
14. Larson AC and Von Dreele RB (1994) General structure analysis system. Report No. LAUR 86-748, Los Alamos National Laboratory, 127 p
15. Bish DL (1989) In: JE Post (ed) Reviews of Mineralogy, vol. 20. Mineralogical Society of America, Washington DC
16. Young RA, Prince E, Sparks RA (1982) J Appl Crystallogr 151:357
17. Mills P, Sullivan JL (1983) J Phys D, Appl Phys 16:723
18. Warren BE (1969) X-ray diffraction. Addison-Wesley, Reading, MA
19. Thompson P, Cox DE, Hastings JB (1987) J Appl Crystallogr 20:79
20. Ramsdell LS, Kohn JA (1951) Acta Crystal 44:111
21. Jahn HA, Teller E (1937) Proc R Soc A 161:220
22. Figgis B, Hitchman MA (2000) Ligand field theory and its applications. Wiley-VCH, 158
23. Fujimura N, Nishihara T, Goto S, Xu J, Ito T (1993) J Crystal Growth 130:269